Energy & Environmental Science

ROYAL SOCIETY OF CHEMISTRY

PAPER

View Article Online
View Journal | View Issue

Cite this: *Energy Environ. Sci.*, 2023, **16**, 1125

A high-energy aqueous Zn‖NO_2 electrochemical cell: a new strategy for NO_2 fixation and electric power generation†

Longtao Ma,[ab] Shengmei Chen,[b] Wenhao Yan,[b] Guobin Zhang,[b] Yiran Ying,[c] Haitao Huang,[c] Derek Ho,*[b] Wei Huang*[a] and Chunyi Zhi*[bd]

Received 21st November 2022,
Accepted 23rd January 2023

DOI: 10.1039/d2ee03749a

rsc.li/ees

Air pollution by nitrogen oxides (NO_2) from exhaust gas is a deep-seated problem, thus urgently calling for new capture and abatement technologies. Meanwhile, the electrocatalytic conversion of NO_2 to value-added chemicals is a promising strategy for mitigating human-caused imbalances of the global nitrogen cycle. Here, we propose an electrochemical cell based on an aqueous Zn‖NO_2 system with a nano-NiO catalyst deposited as the cathode, a metallic Zn foil as the anode and a $ZnCl_2$ aqueous solution as the electrolyte. Importantly, the electrolyte can efficiently capture NO_2, then convert it to NO_2^- and eventually to value-added NH_3, while simultaneously producing electric power. As proof of concept, a battery has been fabricated, which exhibits bifunctional activity and stability (>100 h) towards reversible NO_2 reduction and evolution reactions. A high cell-level energy density of 553.2 W h kg^{-1}_{cell}/1589.6 W h L^{-1}_{cell} from pouch cells (2.4 Ah) has been achieved. As an additional green feature, the produced NO_2^- by the Zn‖NO_2 cell is subsequently converted to NH_3 by a self-powered mechanism, thereby servicing multiple key conversion steps in the nitrogen cycle all within a single device, paving the way to scalable, highly integrated solutions.

Broader context

The emission of industrial waste gases and vehicle exhaust gases (*e.g.* NO_2, NO, SO_2, CO_2, CO) from the massive combustion of fossil fuels leads to the need for elimination of the harmful gases and the generation of clean energy. NO_2 gas causes great harm to the human body, such as damage to eye, nose, throat, and lung tissues. Therefore, the capture and conversion of harmful NO_2 gas to valuable products is of great significance. Metal–gas batteries have been demonstrated to be an effective strategy for efficiently capturing various gases and continuously suppling electrical energy. Zinc metal is an attractive anode material for aqueous batteries, due to its high theoretical capacity (820 mA h g^{-1}), low redox potential (−0.76 V *vs.* SHE), low cost, abundant reserves, and suitable reactivity. By coupling a Zn anode with a NO_2 gas diffusion electrode, the device is capable of performing electrochemical capture and conversion of NO_2. Here, we report a 1.8 V, 2.4-Ah-scale aqueous Zn‖NO_2 electrochemical system with 3 vol% NO_2/air utilized as an energy carrier to store renewable energy, which exhibits an ultrahigh cell level energy density of 553.2 W h kg^{-1}_{cell} and 1589.6 W h L^{-1}_{cell}. The Zn‖NO_2 cells are effective for both capturing NO_2 and converting NO_2 to NO_2^- species at room temperature. The faradaic efficiency of $NO_2 \rightarrow NO_2^-$ reaches 96.4%. The produced NO_2^- can be further converted to NH_3 using an electrochemical Haber–Bosch reactor, self-powered by the Zn‖NO_2 cells.

Introduction

The ever-increasing worldwide energy demand and emission of industrial waste gases and vehicle exhaust gases (*e.g.* NO_2, NO, SO_2, CO_2, CO) from the massive combustion of fossil fuels leads to the need for effective technologies for the capture of exhaust gases and their subsequent conversion into electricity.[1–8] Among them, NO_2 released into the atmosphere contributes to photochemical smog, stratospheric ozone deterioration and global warming, causing serious environmental and health problems.[6,9,10] A strategy is urgently required to convert NO_2,

[a] *Frontiers Science Center for Flexible Electronics, Institute of Flexible Electronics, Northwestern Polytechnical University, Xi'an, 710072, P. R. China. E-mail: iamwhuang@nwpu.edu.cn*
[b] *Department of Materials Science and Engineering, City University of Hong Kong, 83 Tat Chee Avenue, Kowloon, Hong Kong 999077, P. R. China. E-mail: derekho@cityu.edu.hk, cy.zhi@cityu.edu.hk*
[c] *Department of Applied Physics and Research Institute for Smart Energy, The Hong Kong Polytechnic University, Hung Hom, Kowloon, Hong Kong 999077, P. R. China*
[d] *Center for Advanced Nuclear Safety and Sustainable Development, City University of Hong Kong Kowloon, Hong Kong 999077, P. R. China*

† Electronic supplementary information (ESI) available. See DOI: https://doi.org/10.1039/d2ee03749a

which will alleviate NO_2 accumulation and simultaneously produce value-added chemicals such as NH_3.[11–13]

A variety of metal‖gas electrochemical cells, such as Li‖CO_2, Li‖SO_2, Al‖CO_2, and Zn‖CO_2 systems, have been proposed as novel approaches to capture exhaust gas streams while being equipped with the additional benefit of electrical energy production.[14–19] For NO_2 gas, a Li‖NO_2 battery is reported to reduce NO_2.[20] However, the Li‖NO_2 cell produced NO as the final reduzate, which is itself another air pollutant.[21,22] Currently, there is no electrochemical method to capture and utilize exhaust NO_2 to make value-added chemicals, and to simultaneously produce electrical power.

Zinc (Zn) metal is an attractive anode material for aqueous batteries, due to its high theoretical capacity (820 mA h g^{-1}), low redox potential (−0.76 V *vs.* SHE), low cost, abundant reserves, and suitable reactivity.[7,23–28] By coupling a Zn anode with a NO_2 gas diffusion electrode, the device is capable of performing electrochemical capture and conversion of NO_2 with an overall reaction as follows:

$$Zn + 2\ NO_2 \rightarrow Zn(NO_2)_2\ E^0 = 1.85\ V\ (vs.\ Zn/Zn^{2+}) \quad (1)$$

The Zn‖NO_2 electrochemical capture system may be operated in either secondary (rechargeable) or primary (non-rechargeable) modes. In a secondary cell, reduced NO_2 species react with oxidized metal ions to form metal nitrates and electricity during cell discharge (Fig. 1a-i). Ideally, recharging the cell reverses the reaction, consuming electrical energy to release the captured NO_2 at the cathode and regenerating the metal anode. Adoption of a secondary electrochemical process would therefore facilitate the separation and concentration of NO_2 based on the following electrochemical reaction, as demonstrated in Fig. 1a-ii.

$$NO_2^- - e^- \rightarrow NO_2 \quad (2)$$

Another configuration of interest is the primary electrochemical cell, where the metal anode is consumed to produce electrical energy and discharge products, which can be harvested (from the electrode, electrolyte, and other cell components) and converted to valuable chemicals (Fig. 1b) based on the following electrochemical reaction.

$$NO_2^- + 5H^+ + 4e^- \rightarrow NH_3 + 2H_2O \quad (3)$$

Here, we report a 1.8 V, 2.4-Ah-scale aqueous Zn‖NO_2 electrochemical system with 3 vol% NO_2/air utilized as an energy carrier to store renewable energy, which exhibits an ultrahigh cell level energy density of 553.2 W h kg^{-1}_{cell} and 1589.6 W h L^{-1}_{cell}. The Zn‖NO_2 cells are effective for both capturing NO_2 and converting NO_2 to NO_2^- species at room temperature. The faradaic efficiency of $NO_2 \rightarrow NO_2^-$ reaches 96.4%. The produced NO_2^- can be further converted to NH_3 using an electrochemical Haber–Bosch reactor, self-powered by the Zn‖NO_2 cells.

Screening catalysts and analysis of catalytic activity

The screening of the electrocatalytic activity for $NO_2^- \leftrightarrow *NO_2$ conversion ('*' denotes the adsorbed state) on various surfaces of metal oxides, such as NiO, CoO, FeO and CuO, is scrutinized

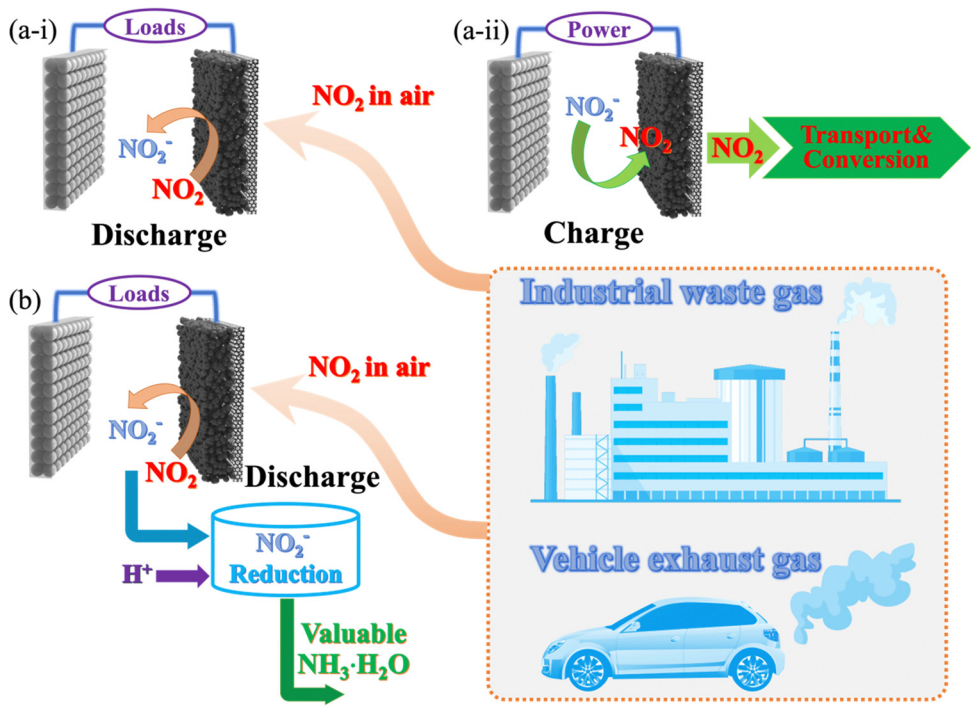

Fig. 1 Architectures of Zn‖NO_2 electrochemistry technology as a capture system. A secondary Zn‖NO_2 electrochemical cell, in which (a-i) NO_2 is reduced to generate electrical energy and (a-ii) NO_2 is concentrated by recharging. (b) A primary Zn‖NO_2 in which the captured NO_2 is converted to NH_3 H_2O valuable products.

and analyzed by density functional theory (DFT) calculations. From density of states (DOS) calculations (Fig. S1, ESI†), the hybridization between the transition metal (Ni, Co, Cu, Fe) 3d and nitrogen/oxygen 2p orbitals at around 2 eV and from −4 to −2.5 eV can be observed, which contributes to the favorable adsorption of NO_2. After comparing two different NO_2 adsorption configurations (Fig. S2, ESI†), we find that on NiO and FeO, $*NO_2$ prefers configuration 1 in which only the N atom binds to metal site, and on CoO and CuO, $*NO_2$ prefers configuration 2 with both N and O binding to adjacent sites. The charge density difference distribution in Fig. 2a and Fig. S3 (ESI†), shows a clear two-way charge transfer between the metal oxides and NO_2, in which charge accumulates in the top/bottom regions of the O atoms and around the metal–N/metal–O bonds, while charge depletion exists around the O atoms. Bader charge analysis suggests that NiO exhibits a relatively smaller value of charge transfer from the surface to $*NO_2$ (0.691 e^-), in line with the charge density difference distribution results. Therefore, NO_2 is weakly trapped on the surface, which facilitates the desorption and the two-way $NO_2^- \leftrightarrow *NO_2$ conversion. The Gibbs free energy diagrams in Fig. 2b suggest that the conversion from $* + NO_2^-$ to $*NO_2$ is energetically favorable, therefore the overall reaction thermodynamics are limited by the NO_2 desorption. Results show that both NiO and CoO exhibit a desorption Gibbs free energy change of 2.35 eV, which is much smaller than that for FeO (5.32 eV) and CuO (5.50 eV). These results indicate that NiO has the best performance for catalyzing $NO_2^- \leftrightarrow *NO_2$ conversion.

To deliver a highly efficient conversion, an electrocatalyst with high activity and selectivity for NO_2RR are a prerequisite. The electrocatalytic activities of NO_2RR are examined using a three-electrode configuration, in which the catalyst deposited carbon fiber cloth (CFC) is the working electrode, Pt foil is the counter electrode and Ag/AgCl is the reference electrode. Excess NO_2 is blown through a gas pump towards the CFC electrode. In general, the NO_2RR polarization curve exhibits similar features to those of the hydrogen evolution reaction (HER), including an onset potential and an overpotential. The electrocatalytic performance of nano-NiO (420 mV for overpotential at 10 mA cm^{-2}) remarkably outperforms commercial Pt/C, CuO, FeO, CoO and NiO catalysts in 2M $ZnCl_2$ aqueous solution (Fig. S4a, ESI†). Meanwhile, the nano-NiO catalyst exhibits the lowest Tafel slope (61.1 mV dec^{-1}) (Fig. 4b), suggesting the superiority of nano-NiO for NO_2RR. Additionally, the NO_2RR behaviors of nano-NiO are examined in different electrolytes of 2M $Zn(OTf)_2$, 2M $ZnSO_4$, 6M KOH and 2M $ZnCl_2$ aqueous solutions. As shown in Fig. S4b and c (ESI†), it shows both the lowest overpotential and Tafel slope in 2M $ZnCl_2$ aqueous solutions, demonstrating the suitability of the $ZnCl_2$ aqueous electrolyte for the NO_2RR. Furthermore, the aqueous Zn‖NO_2 systems are developed by employing metallic Zn as the anode, deposited electrocatalysts on CFC as the cathode and an aqueous solution of $ZnCl_2$ as the electrolyte. As shown in Fig. 2c, when the batteries based on CuO, FeO and commercial Pt/C electrocatalysts, are charged or discharged, they exhibit a very large overpotential or show a quick voltage drop to zero. This observation indicates the very sluggish electrocatalytic kinetics of Zn‖NO_2 batteries using commercial CuO, FeO and Pt/C as catalysts. Although the CoO electrocatalyst enables the Zn‖NO_2

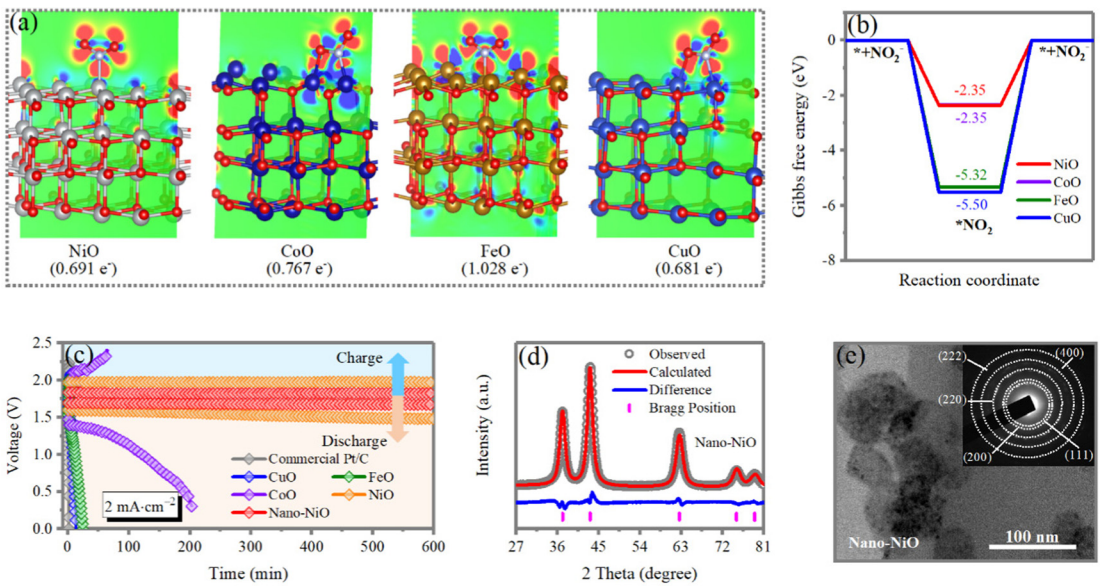

Fig. 2 (a) 2D contour plot (0.005 e $Bohr^{-1}$) of the charge density difference distribution (CDDD) of adsorbed $*NO_2$ on NiO, CoO, FeO and CuO with the iso-surface value of 0.005 e $Bohr^{-3}$. Meanwhile, the number of charge transfers from the metal oxide surface to $*NO_2$ is also denoted. Color code for atoms: Ni: grey; Co: dark blue; Fe: brown; Cu: light blue; O: red; N: cyan. (b) Gibbs free energy diagrams for $NO_2^- \leftrightarrow *NO_2$ conversion on NiO, CoO, FeO, and CuO surfaces. The purple line represents the Gibbs free energy of CoO, which is covered by that of NiO. (c) The galvanostatic charge/discharge curves of the Zn/NO_2 electrochemical cell at a current density of 2 mA cm^{-2} with commercial Pt/C, CuO, FeO, CoO, NiO and nano-NiO electrocatalysts. (d) XRD pattern of nano-NiO and the corresponding results of the Rietveld refinement. Refined parameters are in space group: $R\bar{3}m$; a = 2.97 Å; c = 7.27 Å. (e) TEM image of nano-NiO. The inset is the corresponding SEAD pattern.

battery to operate, the overpotential gradually increases during the charge/discharge processes. Encouragingly, NiO is particularly effective for catalyzing both the reductions of NO_2 and the oxidation of NO_2^-. Nevertheless, the energy efficiency of the Zn‖NO_2 cell is only 76.3%, and the output voltage gradually decreases from 1.55 to 1.46 V after 600 min, indicating the gradually reduced electrocatalytic activity of NiO. Therefore, employing the nano-NiO electrocatalyst, the Zn‖NO_2 battery can steadily and continuously generate electrical power while the NO_2^- is efficiently oxidized. The energy efficiency that is calculated by dividing the discharge voltage by the charging voltage, reaches 92.6% when the NiO nanoparticle (nano-NiO) electrocatalyst is used, which is much higher than that of the well-studied Zn–air batteries (<60%).[29–33] The enhanced electrocatalytic activity is attributed to sufficient active sites and the rapid transport of electrons and ions with the nanostructuration of the NiO electrocatalyst.

To further enhance the catalytic efficiency of NiO, nano-NiO is fabricated *via* an ultrasonic crushing method. The morphology and structure are investigated using X-ray diffraction patterns (XRD), scanning electron microscopy (SEM) and transmission electron microscopy (TEM). The fabricated nano-NiO exhibits well-resolved but broader diffraction peaks with high intensity, indicating small crystallite sizes. The crystal structure is successfully refined with the space group of $R\bar{3}m$ (Fig. 2d), which is similar to that of NiO. The representative SEM image exhibits a uniformly well-defined bean pod-shape with a diameter of ~100 nm (Fig. S5, ESI†). The TEM image depicts a dense bean pod-like structure, and the corresponding selected area electron diffraction (SAED) pattern confirms further its polycrystalline characteristics (Fig. 2e).

Electrochemical performances of Zn‖NO_2 cells

The electrochemical performance of the Zn‖NO_2 batteries-based on nano-NiO is investigated. The linear sweep voltammetry (LSV), open circuit voltage (OCV) and galvanostatic charge/discharge curves are conducted following the protocols well developed by Zn–air battery community. As shown in Fig. 3a, the output voltage of the device with the nano-NiO electrocatalyst exhibits a high OCV of 1.83 V under a NO_2 atmosphere, close to theoretical value of 1.85 V, which is higher than that based on the commercial NiO electrocatalyst (1.75 V). As shown in Fig. 3b, the peak power densities of the Zn‖NO_2 system employing NiO and nano-NiO reach 20.1 and 90.5 mW cm^{-2}, respectively, validating the superior NO_2RR kinetics of nano-NiO. The symmetric charge/discharge curves in Fig. 3c indicate the bifunctional electrocatalysis of nano-NiO for NO_2RR and NO_2^- oxidation, surpassing the counterpart values of the NiO-based cells.

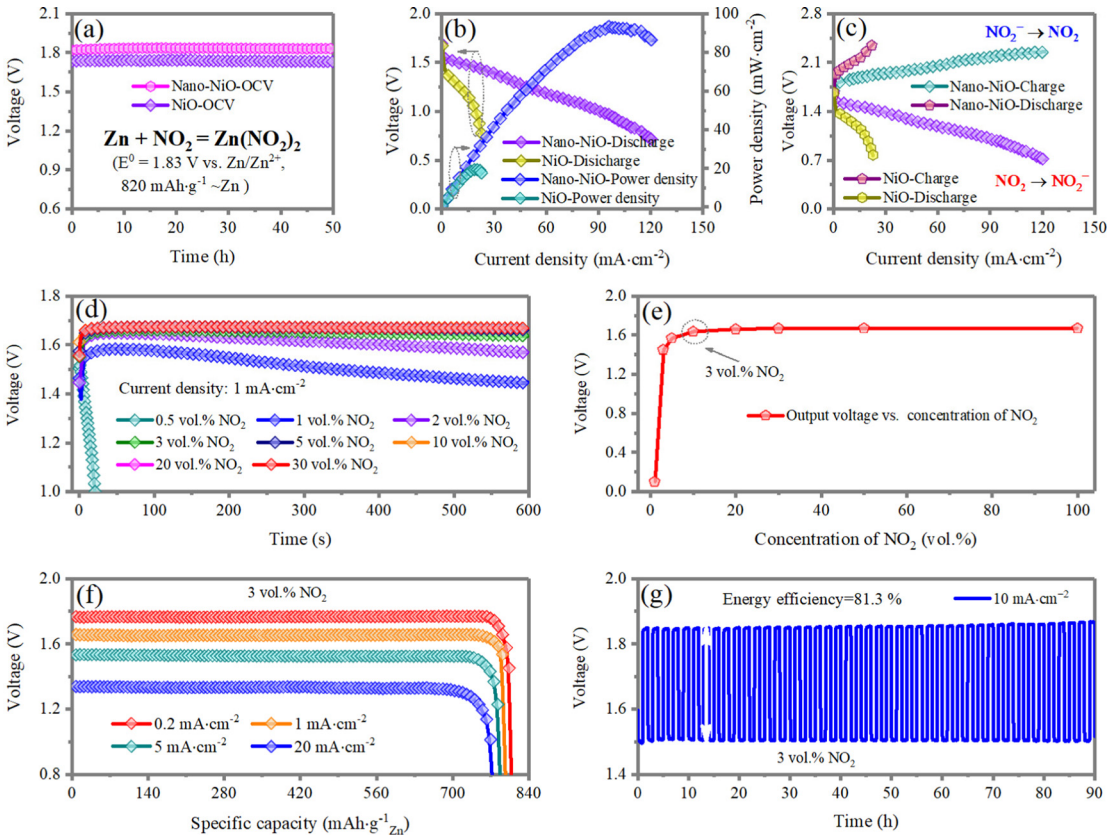

Fig. 3 The Zn‖NO_2 electrochemical cell with NiO and nano-NiO catalysts. (a) Open circuit voltage over 50 h. (b) The discharged polarization profile and corresponding power density curves at different densities. (c) Charge–discharge polarization profiles at different current densities. (d) Full discharged profiles recorded at different current densities of 0.2, 1, 5, 10 mA cm^{-2}. (e) Cycling performance testing at 2 mA cm^{-2} using the nano-NiO catalyst.

For the imitation of the practical application of our design, Zn‖NO_2 systems employing different concentrations of NO_2 gas are studied. It is noted that the mixture of NO_2/air is used to simulate the gas contaminated by NO_2. As shown in Fig. 3d and e, for a NO_2 gas content lower than 3 vol%, the NO_2 gas is depleted with the discharge process, while the Zn‖NO_2 system can steadily and continuously work with >3 vol% NO_2 gas diffusing. Therefore, all subsequent experiments are conducted under the condition of 3 vol% NO_2 gas.

The discharge curves of the Zn‖NO_2 system at different discharge current densities are shown in Fig. 3f. The battery delivers a high specific capacity of 820 mA h g^{-1} with an output voltage of 1.79 V at 0.2 mA cm^{-2}. With the current increased up to 20 mA cm^{-2}, the battery can deliver a high capacity of 753 mA h g^{-1} with 91.8% capacity retention, manifesting an excellent rate capability. The excellent rate capability originates from fast NO_2RR kinetics and the high ionic conductivity of the aqueous electrolyte (47.65 mS cm^{-1}) (Fig. S6, ESI†). In order to exclude the participation of air, we investigate the discharge voltage profile of the Zn‖NO_2 cell at 1 mA cm^{-2} with 3 vol% NO_2/Ar diffused (Fig. S7, ESI†). It is observed that the electrochemical behavior is almost the same, suggesting that only nitrogen dioxide is involved in the electrochemical reaction. Long-term galvanostatic voltage profiles are collected at an absolute current density of 10 mA cm^{-2} with a time span of 1 h for each charging and discharging step. In Fig. 3g, there is almost no polarization increase over 90 h and the phase composition of nano-NiO remains unchanged (Fig. S8, ESI†), validating the stable nano-NiO electrocatalyst in the aqueous system and the high reversibility of the gas cathode based on the NO_2/NO_2^- redox reaction. Furthermore, the changes of the pH value are investigated by a home-made operando pH detection configuration (Fig. S9a, ESI†). The pH value near the gas electrode gradually decreases from 3.96 to 3.49 during the discharge process and is followed by a progressive increase to 3.89 at the charged state (Fig. S9b, ESI†), demonstrating a reversible pH change during the discharge/charge process and thus promoting the cyclic stability.

A 553.2 W h kg^{-1}_{cell}, 2.4 Ah-scale pouch-type Zn‖NO_2 cell

The Ah-scale Zn‖NO_2 cells within a more practical system assembled with a metallic Zn anode are fabricated using a symmetric configuration, wherein the cathodes and electrolytes are positioned on both sides of a metallic Zn anode (Fig. 4a-i and a-ii). The full-cell system can provide an output energy density of 553.2 W h kg^{-1}_{cell} during discharging (calculated based on the mass of total loaded materials on both the electrodes, the electrolyte, and the package, illustrated in the pie chart in Fig. S10, ESI†). The cell-level discharge capacity of 333.3 mA h g^{-1}_{cell} at the current density of 0.2 mA cm^{-2} is recorded with a nominal cell voltage of 1.78 V using ~2.4 Ah full cells (Fig. 4b). No obvious potential drop is observed in the galvanostatic discharging at different current densities (0.2 and 5 mA cm^{-2}) until the Zn plate is exhausted or broken, which indicates good stability in the NO_2RR test. Under realistic conditions (considering all active and inactive components), the Ah-scale Zn‖NO_2 cell achieved ground breaking cell-level specific and volumetric energy densities of 553.2 W h kg^{-1}_{cell} and 1589.6 W h L^{-1}, respectively, based on all active and non-active materials (Fig. S11, ESI†). These are the highest cell energy densities ever reported out of all of commercial Li-ion batteries, Zn-ion batteries and other advanced batteries[34–39] (Fig. 4c). Note that the Ah-scale Zn‖NO_2 cells

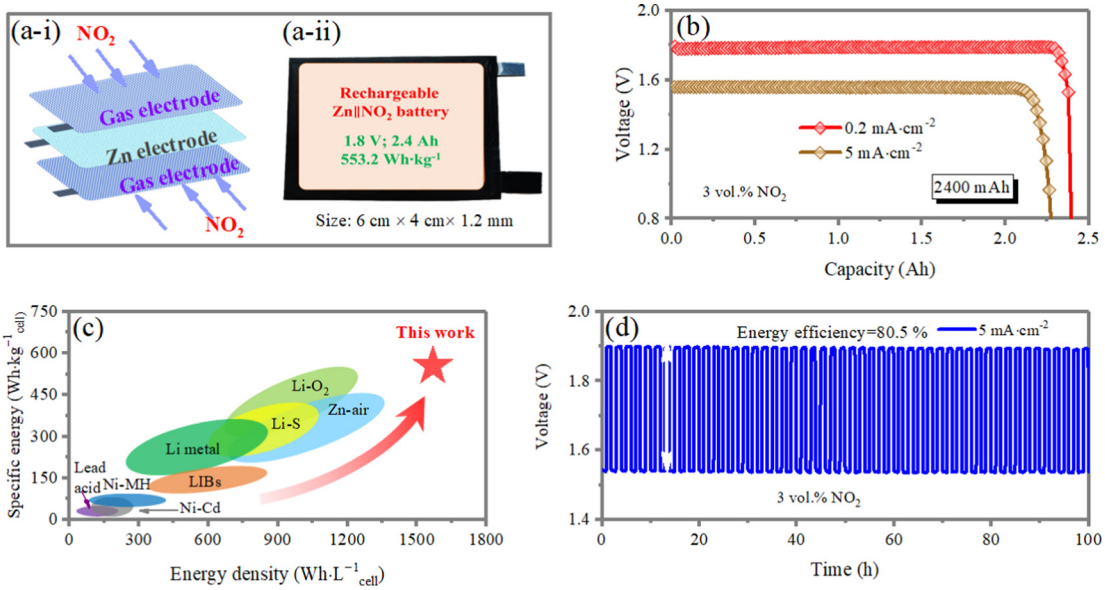

Fig. 4 (a-i) Schematic illustration of a rechargeable aqueous Zn‖NO_2 pouch cell with a cathode-anode-cathode stack structure. (a-ii) An optical photograph of a rechargeable aqueous Zn‖NO_2 pouch cell. (b) The delivered cell capacities of NO_2‖Zn‖NO_2 cells at different rates of 0.2 and 5 mA cm^{-2}. (c) Ragone plots for projected cell-level specific (W h $kg^{-1}_{(cell)}$) and volumetric (W h L^{-1}) energy densities with representative commercial and reported batteries. (d) Galvanostatic cyclic charge/discharge performance of a NO_2‖Zn‖NO_2 cell at a current density of 5 mA cm^{-2}.

demonstrate a cycling stability over 100 h at a current density of 5 mA cm^{-2} (charge/discharge time of 1 h), and the energy efficiency reaches 80.5%, which is better than all reported Zn–air batteries[29–31,33,40,41] (Fig. 4d). The high rechargeability and cyclic stability under practical yet harsh testing conditions indicates exceptional commercialization potential.

Using electrochemical NO_2RR to produce value-added chemicals and fuels offers several advantages over traditional chemical engineering synthesis methods, which include operation under mild reaction conditions such as room temperature and ambient pressure, high energy conversion efficiencies, delocalized production and high adaptability and scalability. Another application of the Zn‖NO_2 systems is the production of value-added NO_2^-, which can be further converted to NH_3.[42,43] Galvanostatic measurements are conducted to electrochemically produce NO_2^- at different current densities for 1 h (Fig. 5a). The quantity of the produced NO_2^- is indirectly determined by a chromogenic reaction method coupled with UV-vis absorption, and the standard calibration curve is shown in Fig. S12 (ESI†). The UV-vis spectra of the produced NO_2^- with different discharge currents are given in Fig. S13a (ESI†), and the corresponding calculated yield of NO_2^- is displayed in Fig. 5b. The yield of NO_2^- reaches 3.42 mM cm^{-2} h^{-1} and the maximum Faraday efficiency (FE) is up to 96.4%. The yield of NO_2^- shows an almost linear increase with respect to the discharging current. Similarly, extending the time for NO_2^- evolution at a current density of

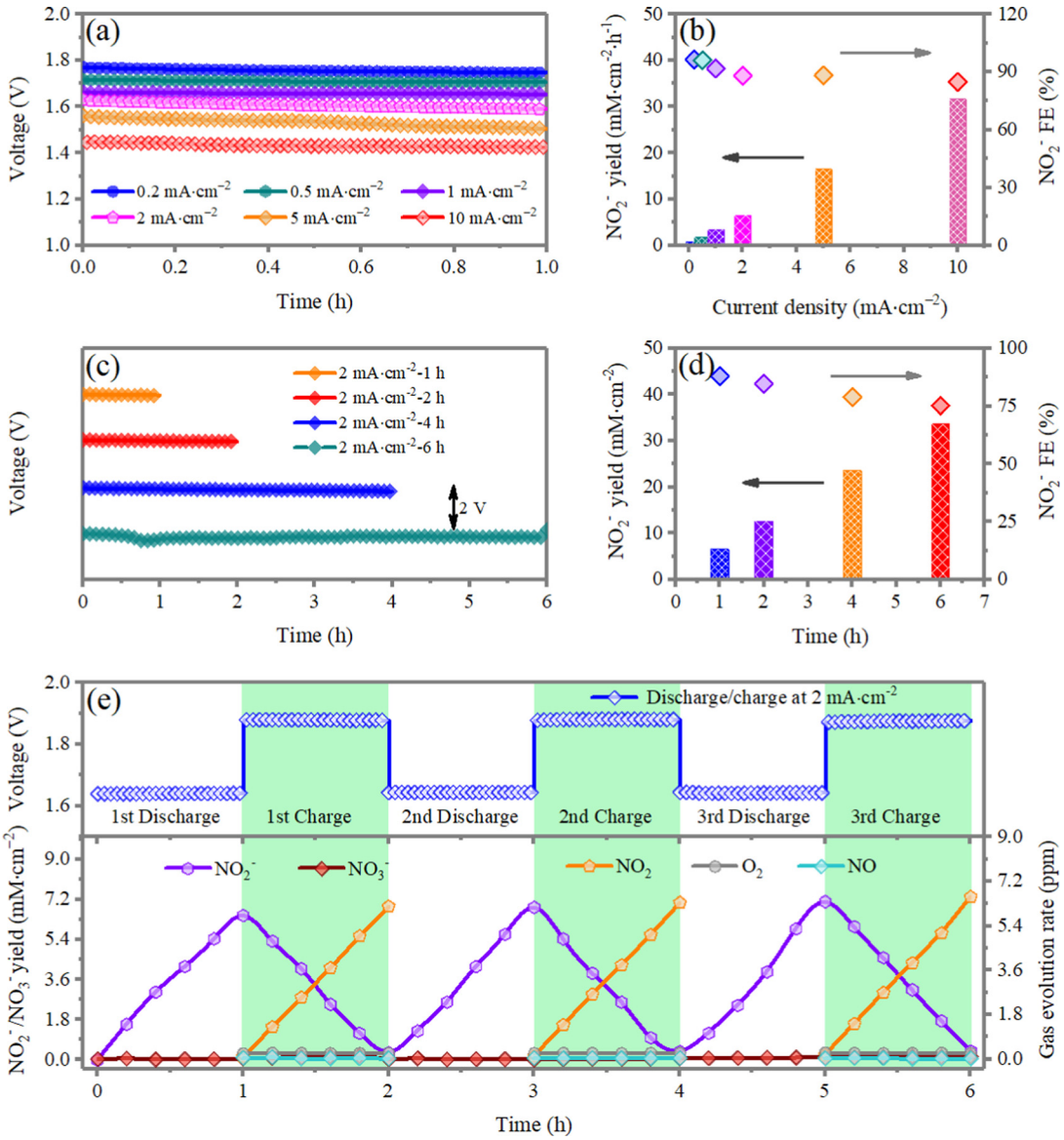

Fig. 5 (a) The galvanostatic discharge profile of a Zn‖NO_2 electrochemical cell at different current densities of 0.2, 0.5, 1, 2, 5, 10 mA cm^{-2}. The length of the black arrows represents 2 V. (b) Corresponding NO_2^- species yield rates and faradaic efficiencies (FE). (c) The galvanostatic discharged profile of a Zn‖NO_2 electrochemical cell over different discharging times of 1, 2, 4, 6 h at 2 mA cm^{-2} and (d) corresponding NO_2^- species yield rates and FE. (e) Discharge–charge curves of first, second and third cycles recorded at 2 mA cm^{-2} over 2 h for one cycle. (f) Discharged/charged time dependence of the NO_2^-, NO_3^-, NO_2, NO, O_2 yield during cycling.

2 mA cm^{-2}, the yield of NO_2^- also shows a linear increase (Fig. 5c, d and Fig. S13b, ESI†). The above results indicate that the Zn‖NO_2 systems can sustain efficient and continuous production of NO_2^-. The slight reduction of FE can be ascribed to the buildup of NO_2^- formed on the surface of the cathode, which reduces the number of catalytic active sites for absorbing NO_2^-. This deficiency can be solved by optimizing the experimental device design, such as adopting a flow cell.

Characterizations are performed to assess the reversibility of the NO_2/NO_2^- interconversion in a closed environment without oxygen/air, which is assumed for the rechargeable Zn‖NO_2 battery system. More accurate quantitative information on both the charge/discharge components and gas evolution have been investigated to further confirm the reaction mechanism and pathway in the Zn‖(3 vol% NO_2 in air) system. As shown in Fig. 5e during repeated cycling, the alternated increasing/decreasing and reversible variation trends of NO_2 and NO_2^-

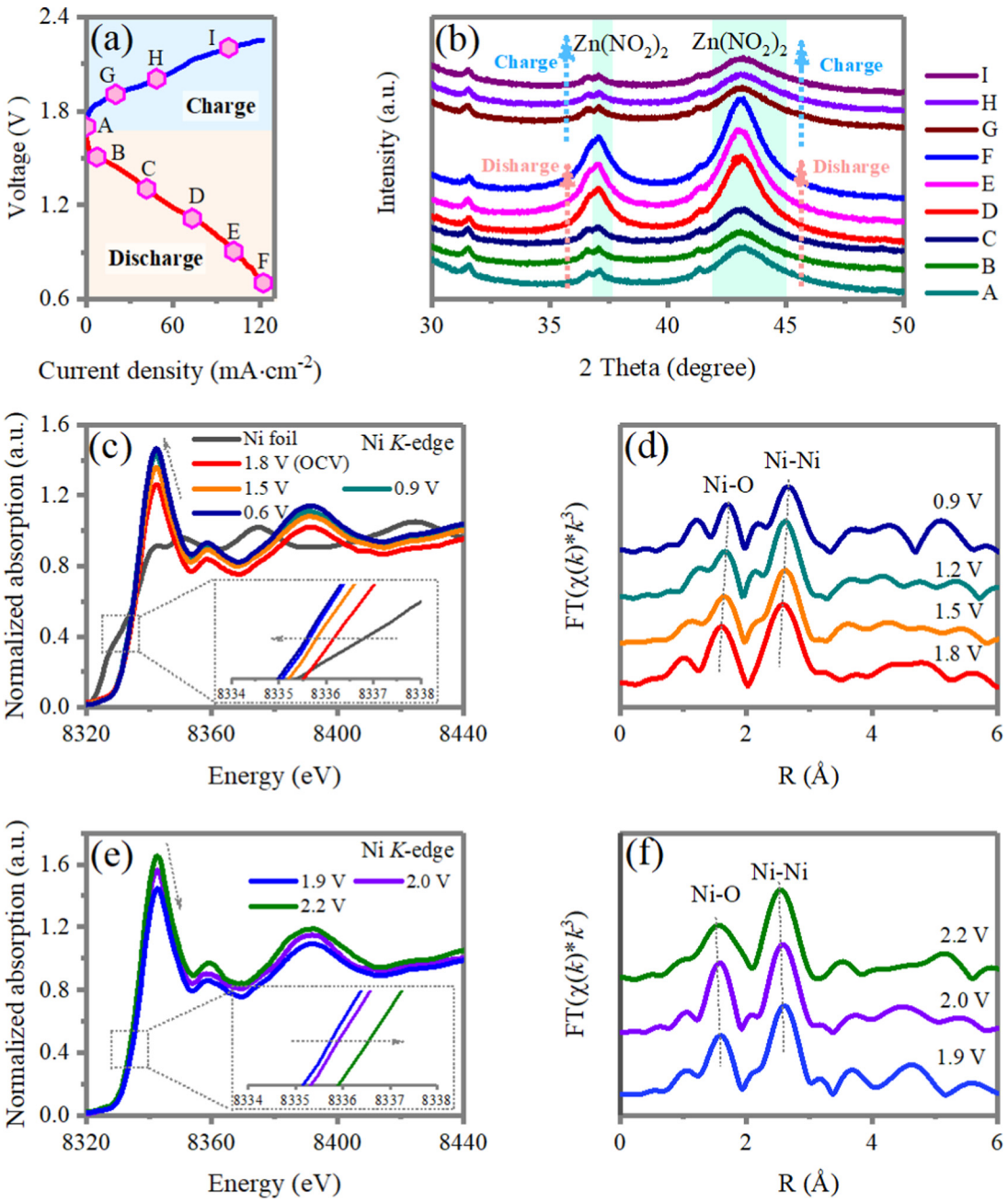

Fig. 6 (a) The charge/discharge curves of a Zn‖NO_2 electrochemical cell and (b) the corresponding *ex situ* XRD patterns of the NiO-deposited gas cathode. (c) Ni K-edge XANES spectra and (d) Fourier-transformed EXAFS spectra collected at the Ni K-edge of the nano-NiO composite obtained *ex situ* at different discharged states. (e) Ni K-edge XANES spectra and (f) Fourier-transformed EXAFS spectra collected at the Ni K-edge of the nano-NiO composite obtained *ex situ* at different charged states.

clearly indicate the reversible interconversion of $NO_2 \leftrightarrow NO_2^-$. In addition, NO_3^-, NO and O_2 signals cannot be observed, which suggests that there are no NO_3^-/NO/O_2 redox processes during the subsequent cycles. The Gibbs free energy change for the $NO_2^- \leftrightarrow *NO_2$ conversion and the oxygen reduction reaction (ORR) at pH = 5 and 7 on NiO are also compared. As depicted in Fig. S14 (ESI†), the $NO_2^- \leftrightarrow *NO_2$ conversion is more favorable than the ORR at both pH values. Both experimental and theoretical results together validate that, although the mixed NO_2/air gas is diffused to the cathode of the Zn‖NO_2 electrochemical cell, there is no O_2/air involved in the redox reactions during the charge and discharge processes.

Structure evolution of the nano-NiO deposited cathode during the $NO_2 \leftrightarrow NO_2^-$ redox process

To unravel the structure evolution of the nano-NiO deposited cathode during the charge/discharge process, *ex situ* X-ray diffraction (XRD), X-ray photoelectron spectroscopy (XPS) and X-ray absorption near-edge spectroscopy (XANES) are performed. As shown in Fig. 6a and b, the discharging process corresponds to Zn^0 losing electrons to form Zn^{2+} ions and the Zn^{2+} first neutralizes the absorbed NO_2^- on the surface of the cathode to form $Zn(NO_2)_2$. Then $Zn(NO_2)_2$ is deposited on the surfaces of the nano-NiO-based gas diffusion electrode. During the charging process, deposited $Zn(NO_2)_2$ on the positive electrode is decomposed, which is confirmed by the absence of $Zn(NO_2)_2$ in X-ray diffraction (XRD) spectrum.

Then, the chemistry of the nano-NiO electrocatalysts are studied by *ex situ* XANES and XPS. Changes in the local electronic and atomic structures of the Ni sites of NiO in the charge/discharge electrocatalytic cycle are monitored by X-ray absorption spectroscopy, including X-ray absorption near edge structure (XANES) and extended X-ray absorption fine structure (EXAFS) analysis. Fig. 6c–f summarizes the Ni K-edge X-ray absorption spectra during electrochemical cycling, including the discharging process from 1.8 to 0.6 V and charging processes from 1.8 to 2.2 V, respectively. With the discharging process (1.8–0.6 V), H_2O is disassociated to H_{ad} and OH_{ad} by breaking the H–OH bond and the absorbed H_{ad} will combine with NO_{2ad} to form HNO_2. The Ni K-edge XANES peaks gradually shift to a lower energy compared with the sample at an open-circuit voltage of 1.8 V, demonstrating a gradually decreased average valence state in NiO[44,45] (Fig. 6c). The results are in line with the XPS results that the Ni $2p_{3/2}$ peaks of NiO after the discharging reaction shift to lower energy, compared with that of pristine NiO (Fig. S15, ESI†). Correspondingly, the Fourier transform of the extended X-ray absorption fine structure (FT-EXAFS) of the interatomic Ni–O distance is enlarged from 1.59 Å to 1.69 Å at an OCV of 0.9 V (Fig. 6d), implying the reduction of the Ni ion with the discharging process. While during the charging process, the H-NO_2^- is broken and dissociated to H_{ad} and NO_{2ad} on the NiO surface. The disassociated H_{ad} will occupy the exposed O site of NiO. The Ni K-edge XANES peaks reversibly shift back to higher energy with the charging process (1.9–2.2 V), indicating an increase in the Ni oxidation state[46,47] (Fig. 6e). Accordingly, the interatomic Ni–O distance is reduced from 1.69 Å at 1.9 to 1.59 Å at 2.2 V (Fig. 3f). The above results support the reversible transitions of the Ni K-edge, manifesting symmetric $Ni^{2+}/^{x+}$ ($1 < x < 2$) redox reactions.

Self-powered Haber–Bosch reactor for NH_3 production

Electrochemical nitrate reduction from NO_2^- into NH_3 is promising for the future landscape of NH_3 electrosynthesis based on the following six-electron reaction:

$$NO_2^- + 7H^+ + 6e^- \rightarrow NH_3 + 2H_2O \quad (4)$$

On the other hand, water electrolysis is a modular alternative H^+ source by using a commercially available water splitting setup, based on the following four-electron reaction:

$$2H_2O - 4e^- \rightarrow O_2 + 4H^+ \quad (5)$$

Based on the above reactions of nitrate reduction and water oxidation, we couple the two reactions into an electrochemical Haber–Bosch (eHB) reactor, which produces NH_3 from NO_2^- and H^+ at ambient conditions in an overall reaction involving only NO_2, H_2O, and renewable electrons. For improving the electrocatalytic kinetics, an effective, cheap and low-toxicity catalyst of commercial nano-TiO_2 (P25) is employed in the electrocatalytic system for NH_3 synthesis. A schematic diagram and an optical photo are depicted in Fig. 7a and Fig. 7b, respectively. The eHB with a dual-compartment electrocatalytic cell, consists of a graphite bipolar plate, a Nafion membrane (NRE-211) and a TiO_2/CFC electrode. The eHB reactor can be powered by two Zn‖NO_2 cells connected in series to drive the subsequent electrocatalytic reduction for NH_3 synthesis. Note that the generated NO_2^- from the Zn‖NO_2 cells can directly flow into the eHB reactor for further NH_3 production. Therefore, as long as we keep providing the electrolyte and NO_2 gas, the self-powered eHB can keep producing NH_3.

Fig. 7c shows the voltage and output current of the electrocatalytic cell. With the duration extended, the voltage maintains 3.0 V unchanged and the output current is about 2.1 mA cm^{-2} over 8 h, demonstrating continuous and stable electrocatalytic reactions for NH_3 synthesis. After 1 h of reaction, NH_3 is successfully synthesized by the self-powered system. The determination results calculated according to UV-vis absorption (Fig. S16, S17, ESI†), are shown in Fig. 7d. By measuring the solution volume involved in the cathode reaction, the self-powered NH_3 yield per hour achieved 4 mM h^{-1}. Therefore, it is feasible to reutilize the residual kinetic energy of the exhaust gas to drive the valuable NH_3 synthesis.

Conclusion

This work presents a high-energy rechargeable aqueous Zn‖NO_2 electrochemical cell, which demonstrates a new

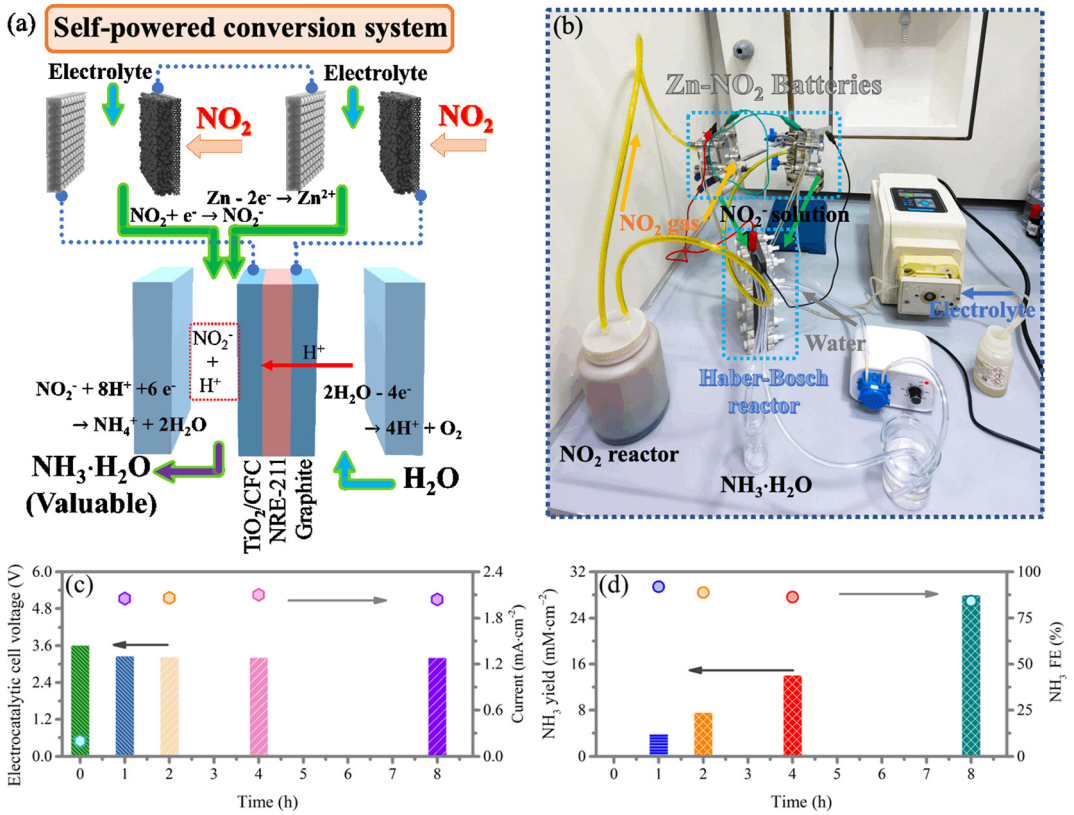

Fig. 7 (a) A schematic of two Zn‖NO_2 electrochemical cell powered electrochemical Haber–Bosch reactor coupled to a water splitting reactor. (b) The corresponding photograph depicting the model. (c) The voltage and current of the electrochemical Haber–Bosch reactor. (d) The NH_3 H_2O yield rates and FE.

approach for converting NO_2 from exhaust gas streams to value-added products while producing large amounts of electrical energy. The aqueous rechargeable Zn‖NO_2 system has a 1.8 V discharge voltage based on reversible NO_2^- ↔ NO_2 conversion, and the energy efficiency reaches 81.3% with 3 vol% NO_2/air diffused at 10 mA cm^{-2}. The assembled pouch-type 2.4 Ah-scale battery can deliver a high energy density of 553.2 W h kg^{-1}_{cell} and a high volumetric density of 1589.6 W h L^{-1}_{cell}. The system is capable of utilizing NO_2 exhaust gas for ammonia synthesis, which is energy-saving and eco-friendly. The yield of the NO_2^- ions reaches 3.42 mM cm^{-2} h^{-1} and the faradaic efficiency is about 96.4%. The produced NO_2^- can be further converted to NH_3 by a self-powered conversion system that consists of two Zn‖NO_2 cells connected in series and an electrochemical Haber–Bosch reactor. This work opens a new avenue for NO_2 capture/conversion *via* reversible aqueous metal‖NO_2 systems and eco-friendly conversion/storage devices.

Author contributions

L. Ma, S. Chen, W. Yan and G. Zhang contributed equally to this work.

Conflicts of interest

There are no conflicts to declare.

Acknowledgements

This research was supported by the National Key R&D Program of China under Project 2019YFA0705104 and the GRF under the project number CityU 11305218. This work was also partially supported by the Fundamental Research Funds for the Central Universities (0515022GH0202253 and 0515022SH0201253), the National Natural Science Foundation of China (52202299) and the Analytical &Testing Center of Northwestern Polytechnical University (2022T006).

References

1 R. C. Armstrong, C. Wolfram, K. P. de Jong, R. Gross, N. S. Lewis, B. Boardman, A. J. Ragauskas, K. Ehrhardt-Martinez, G. Crabtree and M. V. Ramana, *Nat. Energy*, 2016, **1**(1), 15020.
2 M. I. Hoffert, *Science*, 2010, **329**(5997), 1292.
3 R. York, *Nat. Clim. Change*, 2012, **2**(6), 441.
4 D. H. Wall, U. N. Nielsen and J. Six, *Nature*, 2015, **528**(7580), 69.
5 X. Zhang, E. A. Davidson, D. L. Mauzerall, T. D. Searchinger, P. Dumas and Y. Shen, *Nature*, 2015, **528**(7580), 51.
6 S. Shiva, X. Wang, L. A. Ringwood, X. Xu, S. Yuditskaya, V. Annavajjhala, H. Miyajima, N. Hogg, Z. L. Harris and M. T. Gladwin, *Nat. Chem. Biol.*, 2006, **2**(9), 486.

7 Z. Yang, B. Wang, Y. Chen, W. Zhou, H. Li, R. Zhao, X. Li, T. Zhang, F. Bu, Z. Zhao, W. Li, D. Chao and D. Zhao, *Nat. Sci. Rev.*, 2022, nwac268.
8 J. Liu, W. Zhou, R. Zhao, Z. Yang, W. Li, D. Chao, S.-Z. Qiao and D. Zhao, *J. Am. Chem. Soc.*, 2021, **143**(38), 15475.
9 P. M. Edwards, S. S. Brown, J. M. Roberts, R. Ahmadov, R. M. Banta, J. A. deGouw, W. P. Dubé, R. A. Field, J. H. Flynn, J. B. Gilman, M. Graus, D. Helmig, A. Koss, A. O. Langford, B. L. Lefer, B. M. Lerner, R. Li, S. M. Li, S. A. McKeen, S. M. Murphy, D. D. Parrish, C. J. Senff, J. Soltis, J. Stutz, C. Sweeney, C. R. Thompson, M. K. Trainer, C. Tsai, P. R. Veres, R. A. Washenfelder, C. Warneke, R. J. Wild, C. J. Young, B. Yuan and R. Zamora, *Nature*, 2014, **514**(7522), 351.
10 J. O. Lundberg, E. Weitzberg and M. T. Gladwin, *Nat. Rev. Drug Discovery*, 2008, **7**(2), 156.
11 C. H. Christensen, T. Johannessen, R. Z. Sørensen and J. K. Nørskov, *Catal. Today*, 2006, **111**(1), 140.
12 R. Lan, J. T. S. Irvine and S. Tao, *Int. J. Hydrog. Energy*, 2012, **37**(2), 1482.
13 D. Qi, F. Lv, T. Wei, M. Jin, G. Meng, S. Zhang, Q. Liu, W. Liu, D. Ma, M. S. Hamdy, J. Luo and X. Liu, *Nano Res. Energy*, 2022, **1**, e9120022.
14 W. I. A. Sadat and L. A. Archer, *Sci. Adv.*, 2016, **2**(7), e1600968.
15 H. Park, H. D. Lim, H. K. Lim, W. M. Seong, S. Moon, Y. Ko, B. Lee, Y. Bae, H. Kim and K. Kang, *Nat. Commun.*, 2017, **8**(1), 14989.
16 J. Li, L. Wang, Y. Zhao, S. Li, X. Fu, B. Wang and H. Peng, *Adv. Funct. Mater.*, 2020, **30**(27), 2001619.
17 J. Xie, X. Wang, J. Lv, Y. Huang, M. Wu, Y. Wang and J. Yao, *Angew. Chem., Int. Ed.*, 2018, **57**(52), 16996.
18 X. Wang, J. Xie, M. A. Ghausi, J. Lv, Y. Huang, M. Wu, Y. Wang and J. Yao, *Adv. Mater.*, 2019, **31**(17), 1807807.
19 T. Ahmad, S. Liu, M. Sajid, K. Li, M. Ali, L. Liu and W. Chen, *Nano Res. Energy*, 2022, **1**, e9120021.
20 J. Liang, C. Zhang, D. Liu, T. Wu, Y. Tao, G.-W. Ling, H.-J. Yu, J. Lu and Q.-H. Yang, Room-temperature reduction of NO2 in a Li-NO2 battery: a proof of concept, *Sci. Bull.*, 2020, **65**(1), 55.
21 S. W. Bae, S. A. Roh and S. D. Kim, *Chemosphere*, 2006, **65**(1), 170.
22 D. K. Pappas, T. Boningari, P. Boolchand and P. G. Smirniotis, *J. Catal.*, 2016, **334**, 1.
23 F. Wang, O. Borodin, T. Gao, X. Fan, W. Sun, F. Han, A. Faraone, J. A. Dura, K. Xu and C. Wang, *Nat. Mater.*, 2018, **17**(6), 543.
24 J. Zheng, Q. Zhao, T. Tang, J. Yin, C. D. Quilty, G. D. Renderos, X. Liu, Y. Deng, L. Wang, D. C. Bock, C. Jaye, D. Zhang, E. S. Takeuchi, K. J. Takeuchi, A. C. Marschilok and L. A. Archer, *Science*, 2019, **366**(6465), 645.
25 L. Ma, Q. Li, Y. Ying, F. Ma, S. Chen, Y. Li, H. Huang and C. Zhi, *Adv. Mater.*, 2021, **33**(12), 2007406.
26 H. Li, C. Guo, T. Zhang, P. Xue, R. Zhao, W. Zhou, W. Li, A. Elzatahry, D. Zhao and D. Chao, *Nano Lett.*, 2022, **22**(10), 4223.
27 X. Wang, X. Li, H. Fan and L. Ma, *Nano-Micro Lett.*, 2022, **14**(1), 205.
28 X. Li, X. Wang, L. Ma and W. Huang, *Adv. Energy Mater.*, 2022, **12**(37), 2202068.
29 L. Ma, S. Chen, Z. Pei, Y. Huang, G. Liang, F. Mo, Q. Yang, J. Su, Y. Gao, J. A. Zapien and C. Zhi, *ACS Nano*, 2018, **12**(2), 1949.
30 S. Chen, L. Ma, S. Wu, S. Wang, Z. Li, A. A. Emmanuel, M. R. Huqe, C. Zhi and J. A. Zapien, *Adv. Funct. Mater.*, 2020, **30**(10), 1908945.
31 W. Sun, F. Wang, B. Zhang, M. Zhang, V. Küpers, X. Ji, C. Theile, P. Bieker, K. Xu, C. Wang and M. Winter, *Science*, 2021, **371**(6524), 46.
32 J. Pan, Y. Y. Xu, H. Yang, Z. Dong, H. Liu and B. Y. Xia, *Adv. Sci.*, 2018, **5**(4), 1700691.
33 S. S. Shinde, J. Y. Jung, N. K. Wagh, C. H. Lee, D. H. Kim, S. H. Kim, S. U. Lee and J. H. Lee, *Nat. Energy*, 2021, **6**(6), 592.
34 J. H. Kim, Y. H. Lee, S. J. Cho, J. G. Gwon, H. J. Cho, M. Jang, S. Y. Lee and S. Y. Lee, *Energy Environ. Sci.*, 2019, **12**(1), 177.
35 M. Ue, K. Sakaushi and K. Uosaki, *Mater. Horiz.*, 2020, **7**(8), 1937.
36 L. Ma, N. Li, C. Long, B. Dong, D. Fang, Z. Liu, Y. Zhao, X. Li, J. Fan, S. Chen, S. Zhang and C. Zhi, *Adv. Funct. Mater.*, 2019, **29**(46), 1906142.
37 E. Cha, M. Patel, S. Bhoyate, V. Prasad and W. Choi, *Nanoscale Horiz.*, 2020, **5**(5), 808–831.
38 X. Yuan, F. Ma, L. Zuo, J. Wang, N. Yu, Y. Chen, Y. Zhu, Q. Huang, R. Holze, Y. Wu and T. van Ree, *Electrochem. Energy Rev.*, 2021, **4**(1), 1.
39 S. Dühnen, J. Betz, M. Kolek, R. Schmuch, M. Winter and T. Placke, *Small Methods*, 2020, **4**(7), 2000039.
40 L. Ma, S. Chen, D. Wang, Q. Yang, F. Mo, G. Liang, N. Li, H. Zhang, J. A. Zapien and C. Zhi, *Adv. Energy Mater.*, 2019, **9**(12), 1803046.
41 F. Meng, H. Zhong, D. Bao, J. Yan and X. Zhang, *J. Am. Chem. Soc.*, 2016, **138**(32), 10226.
42 K. Han, J. Luo, Y. Feng, L. Xu, W. Tang and Z. L. Wang, *Energy Environ. Sci.*, 2020, **13**(8), 2450.
43 G. F. Chen, Y. Yuan, H. Jiang, S. Y. Ren, L. X. Ding, L. Ma, T. Wu, J. Lu and H. Wang, *Nat. Energy*, 2020, **5**(8), 605.
44 J. Jiang, F. Sun, S. Zhou, W. Hu, H. Zhang, J. Dong, Z. Jiang, J. Zhao, J. Li, W. Yan and M. Wang, *Nat. Commun.*, 2018, **9**(1), 2885.
45 S. Zhao, C. Tan, C. T. He, P. An, F. Xie, S. Jiang, Y. Zhu, K. H. Wu, B. Zhang, H. Li, J. Zhang, Y. Chen, S. Liu, J. Dong and Z. Tang, *Nat. Energy*, 2020, **5**(11), 881.
46 G. F. Chen, T. Y. Ma, Z. Q. Liu, N. Li, Y. Z. Su, K. Davey and S. Z. Qiao, *Adv. Funct. Mater.*, 2016, **26**(19), 3314.
47 H. Doan, I. Kendrick, R. Blanchard, Q. Jia, E. Knecht, A. Freeman, T. Jankins, M. K. Bates and S. Mukerjee, *J. Electrochem. Soc.*, 2021, **168**(8), 084501.

